Marine Pollution Bulletin xxx (xxxx) xxx

Contents lists available at ScienceDirect

Marine Pollution Bulletin

journal homepage: www.elsevier.com/locate/marpolbul

Tracking flood debris using satellite-derived ocean color and particle-tracking modeling

Seongbong Seo [a], Young-Gyu Park [a,*], Kwangseok Kim [b]

[a] Ocean Circulation and Climate Research Center, Korea Institute of Ocean Science and Technology, 385 Haeyang-ro, Yeongdo-gu, Busan Metropolitan City 49111, Republic of Korea

[b] Korea Ocean Satellite Center, Korea Institute of Ocean Science and Technology, 385 Haeyang-ro, Yeongdo-gu, Busan Metropolitan City 49111, Republic of Korea

ARTICLE INFO

Keywords:
Debris
CDOM
TSS
Lagrangian model
Debris hotspot

ABSTRACT

Flood debris associated with Typhoon Lionrock from the Tumen River at the border between Russia and North Korea was traced using ocean color and a Lagrangian particle-tracking model. As debris is transported along with discharged water during floods, a means of tracing floodwater should also allow any associated debris to be tracked. By analyzing the anomalous distribution of colored dissolved organic matter (CDOM) and total suspended sediments (TSS) from the Geostationary Ocean Color Imager (GOCI), the southward movement of the floodwater was tracked along the eastern coast of the Korean Peninsula. This movement was driven by the North Korean Cold Current and was consistent with model results. The similarity between the satellite-derived and modeled datasets shows that CDOM and TSS can be used to track flood-derived debris for several hundreds of kilometers and locate hotspots of debris accumulation.

1. Introduction

On August 31, 2016, Typhoon Lionrock made landfall on Primorsky Krai, Russia, causing heavy rain and flooding along the Tumen River at the border between Russia and North Korea (Fig. 1). The river discharge increased to as high as 13,000 m^3/s during this event (Global Flood Monitoring System; Wu et al., 2014) (Fig. 2), which is significantly higher than the annual mean discharge of approximately 215 m^3/s and the mean August discharge of 560 m^3/s (Tishchenko et al., 2018).

After the flooding, debris consisting of logs and household waste was first reported on September 14, 2016 near Gangneung, South Korea, which is approximately 800 km south of the river (Lee, 2016a). It was estimated that the amount of beached debris was more than 300 tons (Lee, 2016b). This debris had a negative impact on local tourism (Jang et al., 2014), fisheries, and coastal ecosystems (McIlgorm et al., 2011). In addition to the debris reaching the east coast of South Korea, material was likely transported and beached along the coastal of North Korea. In coastal waters, floating logs are hazardous to marine traffic (Hall, 2000). While labels on plastic bottles can be used to determine the origin of ocean debris, near-real-time tracking is indispensable when faced with the potential problems posed by flood-induced debris.

Satellites are a commonly used near-real-time Earth observation tool. When marine debris forms patches with a diameter greater than approximately 10 m, direct detection is possible using high-resolution satellites such as Sentinel-2 (e.g., Biermann et al., 2020; Topouzelis et al., 2019). However, debris that is equal to or smaller than 1 m in diameter is too small to be directly detected using satellites. During flood events, debris can enter the oceans from the mouths of rivers, being transported within floodwaters. Thus, if floodwaters can be effectively traced, so too should any associated debris. Colored Dissolved Organic Matter (hereinafter CDOM for simplicity) and suspended sediment (SS) data from satellites have been used to study freshwater inputs from rivers (Ahn et al., 2008; Bai et al., 2013; Marta-Almeida et al., 2016; Osadchiev, 2015; Warrick et al., 2007), water chemical properties (Del Castillo and Miller, 2008), sediment transport (Choi et al., 2014), and mining wastewater movement (Rudorff et al., 2018). Along with field observations and a Lagrangian particle-tracking model, Atwood et al. (2019) used SS to investigate the coastal accumulation of microplastics from the Po River, Italy. Their satellite-derived results were consistent with their observations and modeling, with the plastic debris mainly accumulating near the river mouth. Atwood et al. (2019) also showed that ocean color information derived from satellites can be used to trace river debris; however, the application of satellite-derived datasets was limited to the areas around river mouths and in open

* Corresponding author.
E-mail address: ypark@kiost.ac.kr (Y.-G. Park).

https://doi.org/10.1016/j.marpolbul.2020.111828
Received 23 June 2020; Received in revised form 19 October 2020; Accepted 2 November 2020

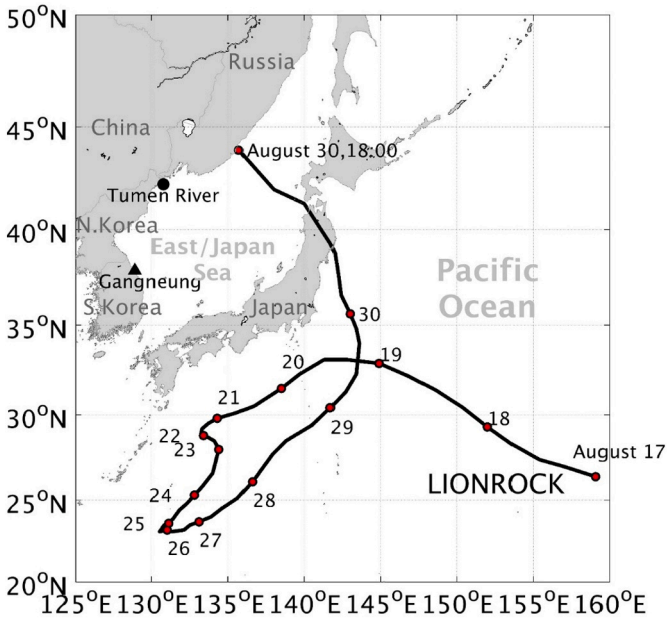

Fig. 1. Track of Typhoon Lionrock, Japan Meteorological Agency. Red dots on the typhoon track are 00:00 (UTC) on each day except the last position (18:00). (For interpretation of the references to color in this figure legend, the reader is referred to the web version of this article.)

water is yet to be tested.

Here, we aimed to trace floodwater and associated debris based on CDOM and Total Suspended Sediments (hereinafter TSS for simplicity) data from the Geostationary Ocean Color Imager (GOCI), which measures the waters around the Korean Peninsula eight times per day. Fluvial inputs affect CDOM and TSS throughout the year, especially during summer. Therefore, mean values were first distinguished from flood-induced anomalies. Such anomalies were then used to trace the flood-induced debris. We take a similar approach to Atwood et al. (2019) by using ocean color information derived from satellite observations. However, to the best of our knowledge, this is the first study to trace flood-derived debris in the open ocean using CDOM and TSS over distances of several hundred kilometers.

Lagrangian particle-tracking models are widely used for tracing floating debris, in which the trajectories of floating objects are calculated based on ocean currents and winds at a regional (Atwood et al., 2019; Critchell et al., 2015; Mansui et al., 2015; Neumann et al., 2014; Yoon et al., 2010) and global scale (Eriksen et al., 2014; Lebreton et al., 2012; van Sebille et al., 2015). In previous studies, the main focus has been the continuous and long-term behavior of debris from a diverse range of sources, while episodic events such as floods have not been the main interest. When modeling floods, it is important to note that a considerable amount of material can be released over a relatively short period of time. Some studies have examined flood-induced debris around the Korean Peninsula including Kim and Yoon (2009) and Yoo et al. (2007); however, these studies focused on river mouths during the first few days following flood events, and the model results were not verified.

Here, we use Lagrangian particle-tracking modeling to trace the debris entering the ocean from the Tumen River following Typhoon Lionrock while simultaneously accounting for river discharge. We compare the model results against the distributions of anomalous CDOM and TSS to test the validity of using these satellite-derived variables as proxies for floating debris. The coastal beaching of the debris is also investigated. Section 2 explains the procedures used to process the satellite data, the derivation of CDOM and TSS anomalies, and the Lagrangian simulations. In Section 3, the anomalous CDOM and TSS distributions are analyzed to identify the flood signal. We then use Lagrangian simulations to trace the flood-derived river debris in comparison to the satellite data. Finally, Section 4 provides a summary and conclusions for the study. Overall, we demonstrate that CDOM and TSS can be used to effectively trace floodwater and associated debris for hundreds of kilometers. In combination with particle-tracking models, this approach allows us to track flood debris and the identification of hotspots of debris accumulation.

2. Methods

2.1. Satellite data-processing

The GOCI that was launched on 27 June 2010 is the first geostationary ocean color satellite. The GOCI collects images around the Korean Peninsula eight times per day between 00:15 and 07:34 GMT (Ryu et al., 2012). The images are processed through the GOCI Data Processing System based on the standard Korea Ocean Satellite Center (KOSC) algorithm (Ahn et al., 2012) to produce GOCI Level 2A (L2A) data three times per day (02:15, 03:15 and 04:15 UTC) with a spatial resolution of approximately 500 m. For this study, L2A CDOM and TSS datasets for August and September for the period 2011–2016 were obtained from the KOSC (http://kosc.kiost.ac.kr).

Both CDOM and TSS images taken on September 6 and 14 (Fig. 3) show a plume moving southward along the coast. To determine if this is a typical feature or was caused by the flooding following Typhoon Lionrock, we decomposed the satellite data into daily climatological means and anomalies. When constructing the daily climatological mean, data between 2011 and 2015 were utilized. Data for 2016 were excluded for two reasons. First, a climatological mean that included data from the event of interest needed to be avoided and, second, 2016 was a relatively unusual year due to the flooding. Given the relatively short record available to us, excluding 2016 as an extreme year also minimized the

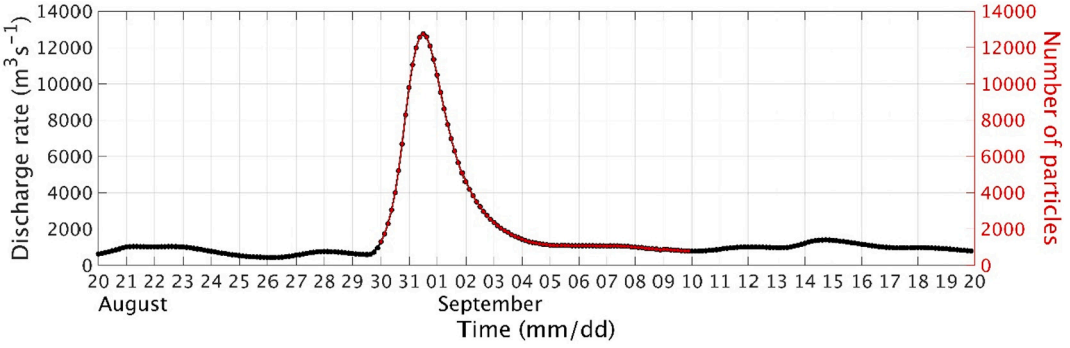

Fig. 2. Tumen River discharge rate from the Global Flood Monitoring System (Wu et al., 2014) (black dotted line), and the number of particles discharged in the model (red dotted line). (For interpretation of the references to color in this figure legend, the reader is referred to the web version of this article.)

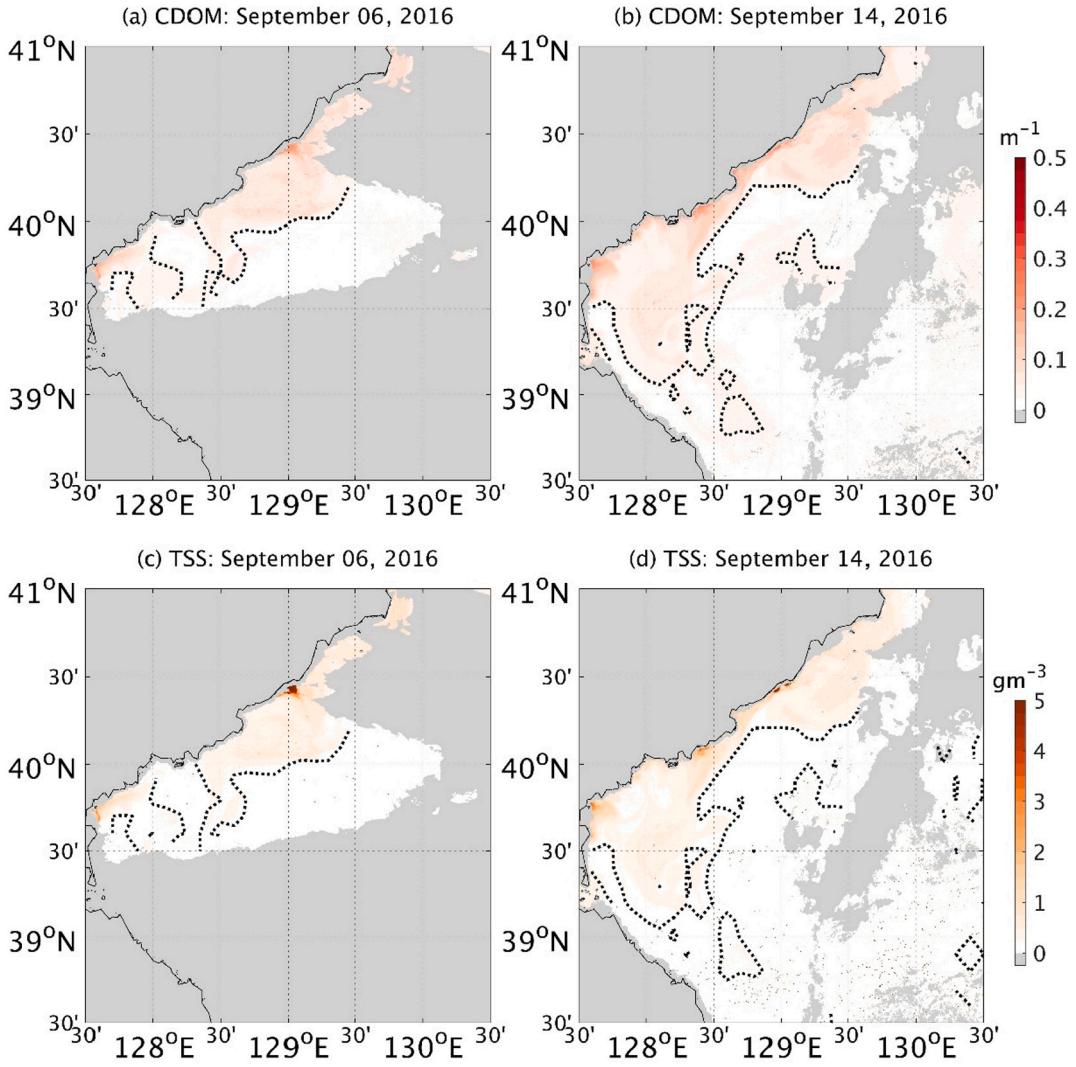

Fig. 3. CDOM and TSS on September 6 and 14, 2016. The contour lines represent e-folding scale for each quantity (0.03 m^{-1} for CDOM, and 0.17 gm^{-3} for TSS). Light gray shading is for the areas covered by cloud or sea fog.

likelihood of bias. To derive the daily mean conditions, first a daily composite was constructed using the three daily L2A datasets followed by a 16-day running mean to remove cloud effects (Kwan et al., 2016). Using this daily time-series, the daily climatological mean was derived. The differences between the daily mean conditions and the daily time-series in September 2016 were then defined as anomalous CDOM and TSS distributions. Due to cloud the anomalies could not be traced continuously and the model results were used to fill the gaps.

2.2. Lagrangian particle-tracking model

The model utilized here was the same as that employed by Seo and Park (2020), as follows:

$$\vec{x}_{t+\Delta t} = \vec{x}_t + \int_t^{t+\Delta t} \left\{ \vec{u}_c\left(\vec{x}_t, \tau\right) + W_f \times \vec{w}_{10m}\left(\vec{x}_t, \tau\right) \right\} d\tau + R\sqrt{2K_h\Delta t}$$

where $\vec{x}_t$ is the position of a particle at time t; Δt is the time interval (3 h); $\vec{u}_c$ and $\vec{w}_{10m}$ are the surface ocean current and wind at 10 m above sea level, respectively; $W_f \times \vec{w}_{10m}$ is the wind drift, where W_f is the windage coefficient, which is commonly referred to as the wind drift factor or the wind effect. The input data were linearly interpolated to particle positions and model time steps. The Runge-Kutta 4th order scheme (Dormand and Prince, 1980) was used for time integration. For completely submerged objects such as small plastic fragments, the windage is 0%. For highly exposed objects such as empty capped plastic bottles and fishing buoys, this increases to 4–5% (Lebreton et al., 2018; Maximenko et al., 2015; Neumann et al., 2014; Yoon et al., 2010); and $R\sqrt{2K_h\Delta t}$ is a random walk component used to simulate unresolved processes and sub-grid-scale turbulent motion (North et al., 2006). R is a random number between −1 and 1, and K_h is a horizontal diffusion coefficient taken from the Smagorinsky (1963) mixing scheme (Choi et al., 2018; Iwasaki et al., 2017).

Similar to Isobe et al. (2009), a beaching criterion of a particle was set based on the semidiurnal tidal cycle and the grid structure. As tidal currents were not explicitly included in our calculations, a beaching zone of 1/60° was set along the coast. The width of this zone is similar to the distance a particle would move due to semidiurnal tidal currents during a half semidiurnal tidal cycle. Particles that remain continuously within the beaching zone for more than 12 h were classified as beached.

2.3. Numerical experiment

The daily 1/12° global field from the HYbrid Coordinate Ocean Model (HYCOM, GOFS 3.0, https://www.hycom.org) output was used for the ocean current component, $\vec{u}_c$. Diverse observation data such as satellite altimeter, sea surface temperature, and profiles from Argo floats

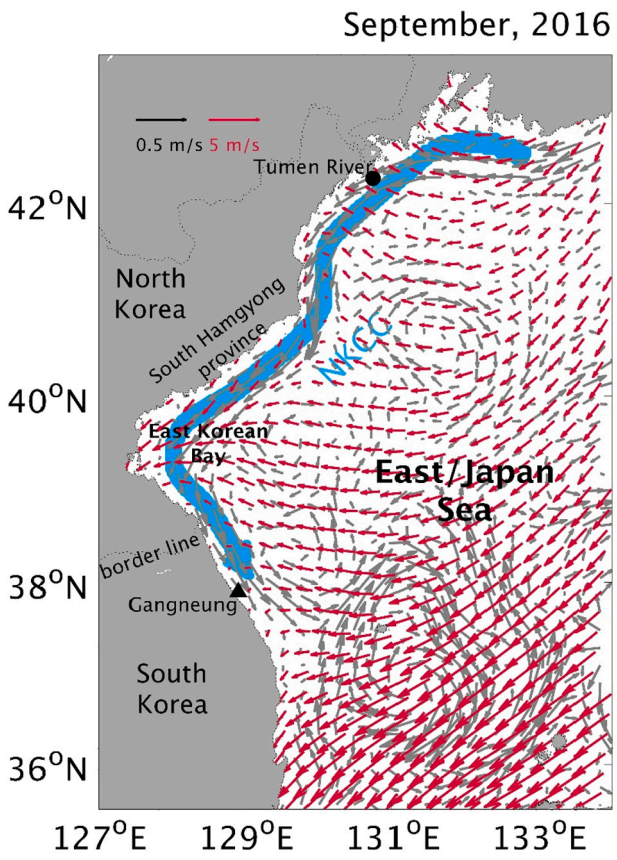

Fig. 4. Mean ocean circulation in the HYCOM (gray arrows) and 10 m wind from the Unified Model (red arrows) during September 2016. Thick light-blue arrows indicate the schematic pattern of the North Korea Cold Current. Black colored dots and triangles indicate the location of the Tumen River mouth and Gangneung, respectively. (For interpretation of the references to color in this figure legend, the reader is referred to the web version of this article.)

are assimilated into the HYCOM. For the 10-m wind component, $\vec{w}_{10m}$, the daily Unified Model (UM) 12-km regional forecast data were obtained from the Korea Meteorological Administration. The mean current and wind patterns for September 2016 are presented in Fig. 4.

The most important flow near the Tumen River mouth is the North Korea Cold Current (NKCC), a southward flow along the North Korean coast that is an extension of the Liman Cold Current flowing south along the Russian coast (Isobe and Isoda, 1997; Yoon and Kim, 2009). As shown in Fig. 4, the NKCC flows eastward to form a subpolar front after encountering the East Korea Warm Current (EKWC) from the south (Seung and Kim, 1989). Therefore, debris from the Tumen River is expected to move southward along the coast, driven by the NKCC.

Wind speeds are low along the coast relative to the open ocean. The direction of the wind near the coast shows latitudinal variations. The wind blows toward the coast around the Tumen River; to the south of the river (between 40°N and 41°N), the dominant winds blow southwestward; in East Korean Bay (between 39°N and 40°N), the winds blow strongly toward the coast; and south of East Korean Bay, the winds still blow toward the coast but the strength weakens to approximately 38°N before strengthening again.

The debris found along the east coast of South Korea is composed of various materials including plastic, logs, and household waste with diverse buoyancy properties. To reflect the diversity of debris types, nine simulations were conducted by varying windage values (W_f) between 0% and 4% at 0.5% increments (Duhec et al., 2015). The exact amount of debris discharged by the flood could not be determined but is expected to be proportional to the discharge rate. Thus, the number of discharged particles was set as being proportional to the river discharge rate (Fig. 2). Thus, the model assumed that particles were discharged every 3 h between August 30 and September 6, with a total of 257,000 particles in each simulation. The particle trajectories were calculated up until October 20. The ocean grids where the particles were released were positioned adjacent to the land grids, and to prevent beaching immediately after their release, the model deflects particles to the ocean when they enter a land grid within one day after their release. Unless river plumes are explicitly resolved, the trick is practically necessary.

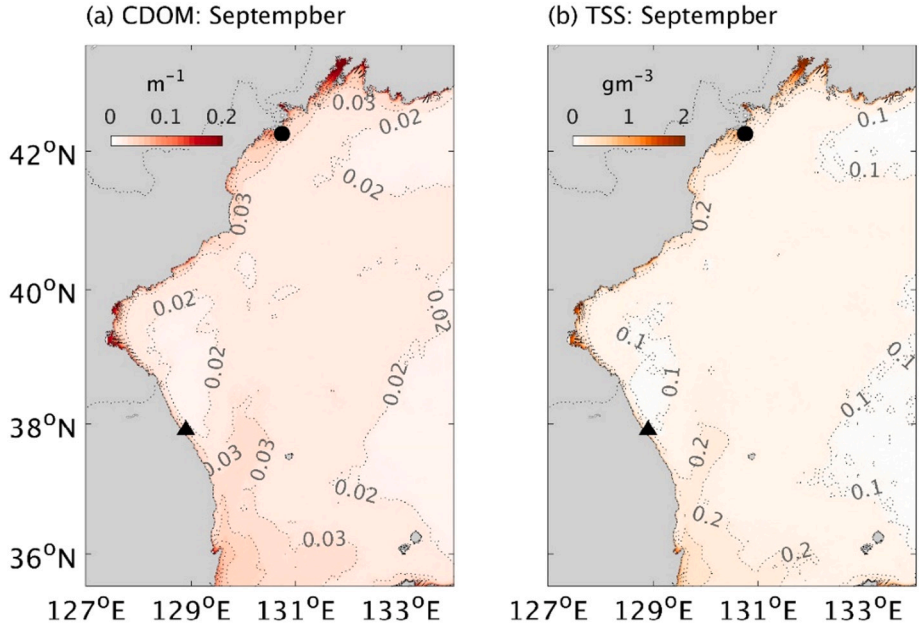

Fig. 5. Mean CDOM (a) and TSS (b) in September for the period 2011–2015.

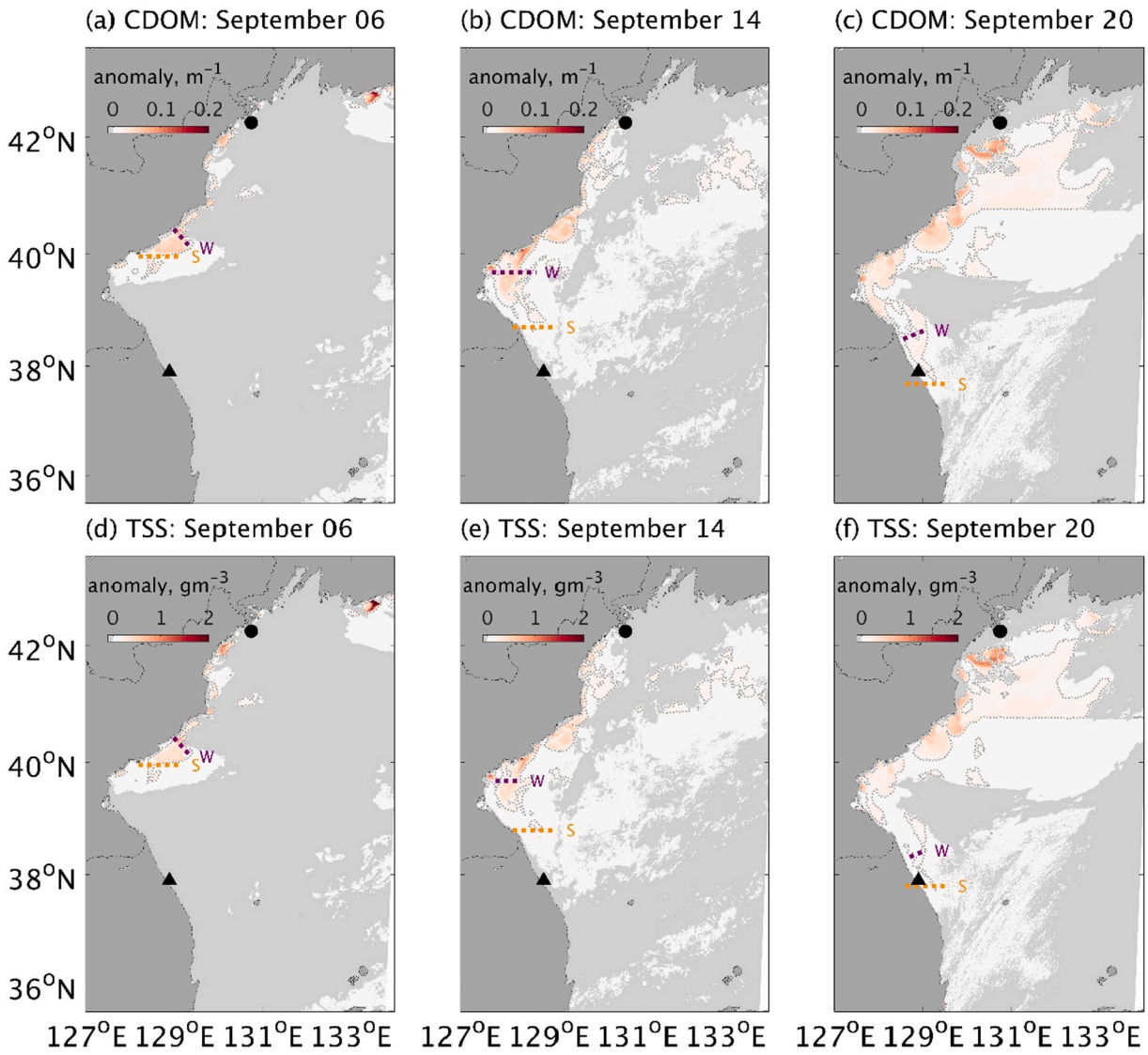

Fig. 6. CDOM (a–c) and TSS (d–f) anomalies immediately after the flood pulse (for September 6), on the date debris beached in Gangneung (September 14), and on September 20. Purple- and orange-colored dotted lines indicate the maximum widths of the southernmost positive anomaly patch perpendicular to the coast and their southern limits, respectively. Light gray shading is for the areas covered by cloud or sea fog. (For interpretation of the references to color in this figure legend, the reader is referred to the web version of this article.)

Table 1
Latitudes of the southern edge and the maximum widths of the southernmost positive anomalies in satellite data (Fig. 6) and model results (Fig. 7) for selected dates.

		CDOM	TSS	Model results (0% windage)	Model results (composite)
September 6, 2016	Latitude	40°N	40°N	40°10′N	40°10′N
	Width (km)	49	49	27	38
September 14, 2016	Latitude	38°42′N	38°48′N	39°N	37°44′N
	Width (km)	85	50	27	36
September 20, 2016	Latitude	37°40′N	37°50′N	38°N	36°33′N
	Width (km)	48	35	20	29

3. Results and discussion

3.1. CDOM and TSS

Fig. 5 shows the mean distribution of CDOM and TSS between September 2011 and 2015. In both cases, high values were found near the river mouth and the innermost part of East Korea Bay. There are small rivers around Vladivostok, and CDOM and TSS show high values. CDOM and TSS values were higher near the coast and, excluding the isolated high values in East Korea Bay, decreased from the river mouth southward along the coast. The ranges of higher values (e.g., 0.03 m^{-1} for CDOM and 0.2 gm^{-3} for TSS) were largest near the mouth of the Tumen River (approximately 50 km) and decreased 10 km south to approximately 40°N. Thus, the patterns of CDOM and TSS reflect southward transport along the coast under the influence of the NKCC (Fig. 4).

Fig. 6 shows CDOM and TSS anomalies on September 6, 2016 immediately after the flooding occurred, on September 14 when debris was first reported in Gangneung, South Korea, and on September 20. As the flooding would have increased CDOM and TSS (Marta-Almeida

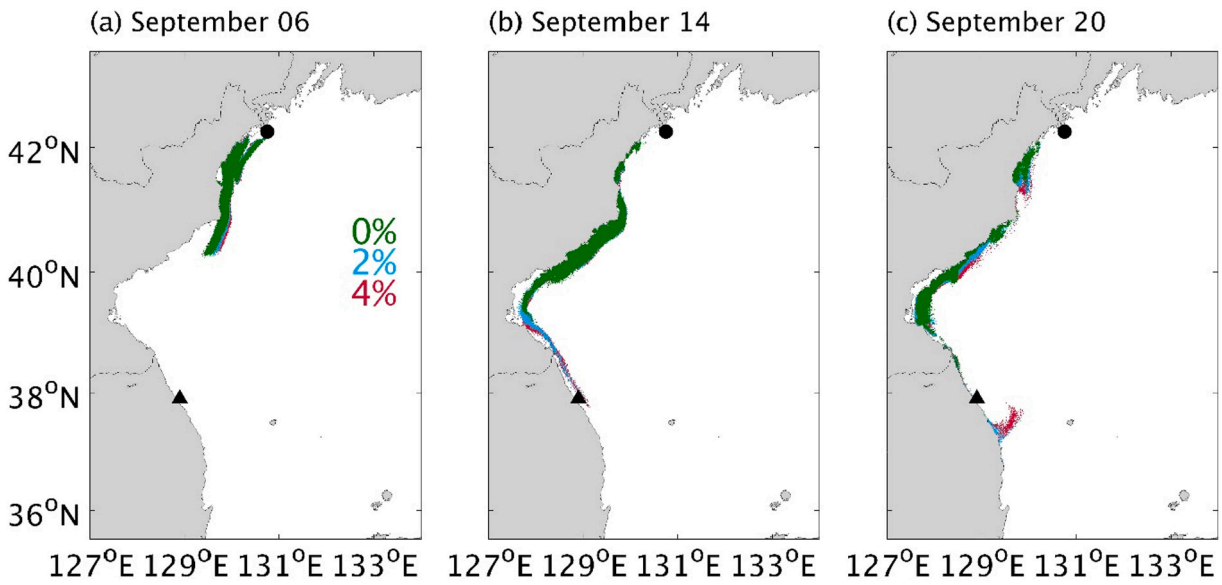

Fig. 7. Modeled particle transport with windage of 0%, 2%, and 4% on September 6 (a), September 14 (b), and September 20 (c).

et al., 2016; Warrick et al., 2007), only positive values are shown. The dotted line in each figure represents 0.01 m^{-1} (CDOM) and 0.08 gm^{-3} (TSS) using an exponential decay scale. In both cases, anomalous values are distributed along the coast following the path of the NKCC. Due to cloud, the light gray shading, the anomalies could be traced back to the river continuously, but one can see that the anomalies were from the north. In images obtained a few days before the flooding, there are no anomalies along the Korean coast. Since Korea was not affect by the typhoon, the anomalies cannot be locally generated. Thus, it is logical to postulate that the anomalies were from the Tumen River where flooding occurred. Since we do not have continues images due to cloud, we compared the satellite images with our model results to prove the postulation.

The leading edges of the anomalies reached South Hamgyong Province (40°N) on September 6, the border between North Korea and South Korea (38.5°N) on September 14, and Gangneung on September 20 (Table 1). As the debris was first noted at Gangneung on September 14, CDOM and TSS transport was slower than the debris transport. This difference was likely due to wind effects acting on the debris as explained in Section 3.3. The maximum widths of the leading CDOM and TSS patches moving along the coast were also compared. On all three dates, the sizes of the patches were comparable between the two variables (Table 1). However, the TSS patches became smaller over time, which was particularly noticeable on September 20 when the area covered by the TSS patch was reduced to approximately 65% of CDOM area.

The suspended sediments discharged from the river would have gradually sunk where the current was weak (Baeye et al., 2016; Burenkov et al., 2010; Choi et al., 2014) and the TSS anomalies became fainter further down the coast. CDOM can also be reduced by photochemistry (Osburn et al., 2009; Vodacek et al., 1997) and microbial activity (Nelson et al., 1998), although the resulting changes are not as significant for TSS. Warrick et al. (2007) showed that CDOM is more correlated with the salinity of storm-induced river plumes than TSS based on vessel-based sampling, and suggested that CDOM is a more reliable tracer of freshwater discharge. Here, we only compared the extent of the plumes, and both CDOM and TSS can be used in tracing freshwater discharge. In comparison to previous work, such as Warrick et al. (2007) who examined flows near a river mouth, our analysis shows tracking data over a distance of several hundreds of kilometers along the NKCC flow path.

3.2. Particle trajectories from the model

The simulated trajectories of the particles from the river are displayed in Fig. 7 for the same dates as the CDOM and TSS anomalies based on windage values of 0%, 2%, and 4%. Irrespective of windage, the particles moved south along the coast due to the NKCC. The windage makes two contributions. First, there is a wind component parallel to the NKCC at 40°N, as can be seen in Fig. 4, and the wind accelerates the southward movement of the particles. Thus, on September 6, the three windage scenarios show similar distributions. On subsequent days, after passing 40°N, the difference between the scenarios becomes more pronounced. On September 14, the southern limits in the 0%, 2%, and 4% scenarios were 39°N, 37°50′N, and 37°44′N, respectively; on September 20, these limits were 38°N, 36°34′N, and 36°33′N, respectively. However, due to the complex interplay between wind and the small eddy in the East Korea Bay, south of 39°N, the difference between the 2% and 4% scenarios was small. The second effect of windage is offshore dispersion. Although the mean wind direction is onshore, offshore winds do occasionally occur. This intensifies with windage along South Hamgyong Province, as can be seen in Fig. 7c. This effect is minor, however, in that the main trajectories did not alter during the 53-day simulation period.

According to local media, a floating debris patch arrived at Gangneung on September 14. On this date in the simulation, no particles had arrived at this location with 0% windage but had arrived in the higher windage (2% to 4%) scenarios. Indeed, the debris reported at Gangneung on this date was composed of logs and plastic bottles, which have high windage, while objects with smaller windage likely arrived later, although there are no observational data to validate this.

3.3. Comparison of satellite data and model results

Considering the diversity of the debris from the river, a composite of all eight cases in which windage was varied between 0% to 4% at 0.5% increments was constructed and compared with the satellite images (Fig. 8). As CDOM and TSS are properties of the water and are not influenced by windage, a 0% windage scenario was also used in the comparison. Importantly, the model produced continuous results while the satellite images were only available for certain dates due to cloud cover. The model results could be used in filling the gaps between the satellite images while the latter validating the former. As can be seen in Figs. 6, 7, and 8, the satellite anomalies and the model results are

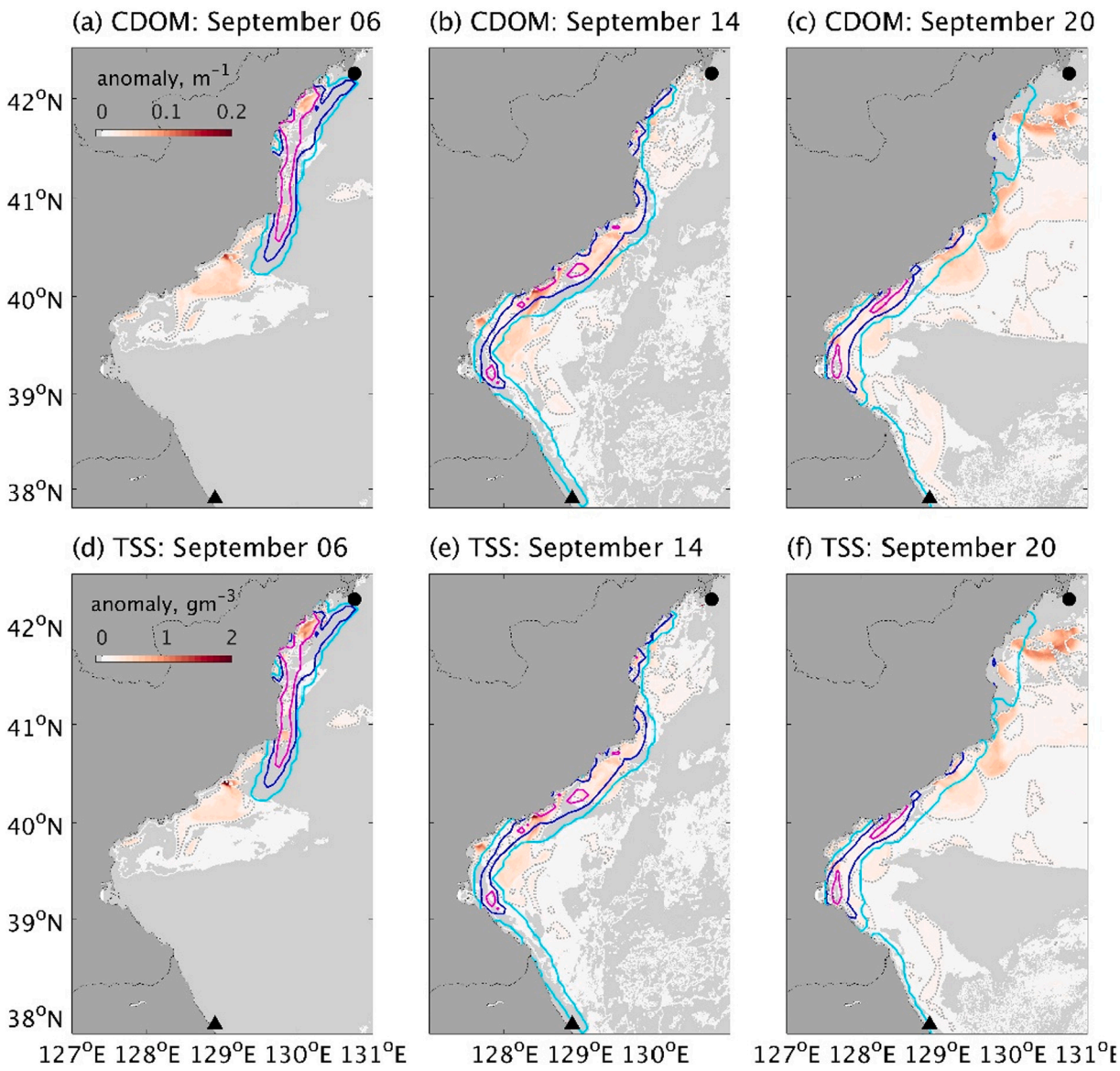

Fig. 8. Comparison of CDOM and TSS anomalies shown in Fig. 6 and particle density from the composite analysis. Cyan, blue, and magenta contour lines are for 0.001, 0.1 and 0.5% particle density, respectively. Light gray shading is for the areas covered by cloud or sea fog. (For interpretation of the references to color in this figure legend, the reader is referred to the web version of this article.)

similar, with the leading edges moving southward along the coast. Note that the distribution patterns of the anomalies were not as continuous as that of the modeled particle plumes as can be seen from Fig. 8 because of small eddies along the coast and apparently due to cloud especially on September 6. For episodic events, the most important factor is the initial arrival time of debris and, therefore, the comparison was made based on the southern limit and the maximum width of the leading plume. When estimating the southern limit from the model results, particles that were separated from other particles by a distance greater than the spatial resolution of the input data (i.e., 0.08°) were excluded.

As listed in Table 1, on September 6, 2016, the composite and 0% windage scenarios show similar southern limits, at approximately 40°10′N, because the time since the initial flood pulse was too short for the effects of the wind to become noticeable. The difference between the two scenarios increases over time, so that on September 14, the difference in the leading edge was approximately 1°20′. Note that on September 20, the difference was approximately the same as on September 14 because the particles started to move offshore along the polar front. The leading edges of CDOM and TSS—both of which moved at a similar rate—are described in Table 1 and were positioned near the 0% windage scenario. For the satellite data and the 0% scenario, it took approximately 20 days for the leading edge to reach Gangneung from the river mouth compared to 14 days in the composite data.

Although comparable, the leading edge of the debris stream in the 0% windage scenario was slower than that derived from the CDOM and TSS data. In the HYCOM model, river discharge is not simulated explicitly but is derived from climatological data (Fournier et al., 2016; Wang et al., 2018). Thus, the model cannot reproduce the alongshore flows resulting from freshwater inputs, meaning the movement of debris was somewhat restricted under the 0% windage scenario (Troselj et al., 2017; Urakawa et al., 2015).

The maximum widths of the leading edges in the offshore direction on the selected dates are also listed in Table 1. In all cases, the widths were comparable to that of the NKCC (approximately 50 km) but the widths in the model results were narrower than those in the satellite images. Freshwater plumes form a tongue at the river mouth (Isobe, 2005), which transports materials in the offshore direction. As this phenomenon is not simulated by the model, the debris could not be

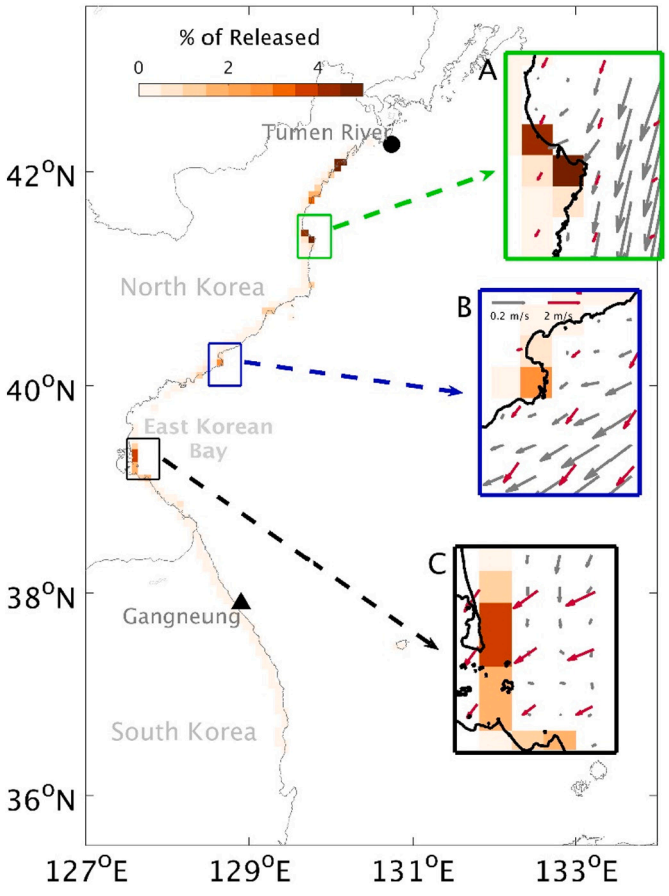

Fig. 9. Distribution of beached particles in the composite analysis. All particles beached up to October 20 (50 days after the initiation of the experiment) are included. The three colored boxes (A, B, and C) indicate beaching hotspots, and the gray and red vectors indicate the mean ocean current and wind directions in each case during September 2016. (For interpretation of the references to color in this figure legend, the reader is referred to the web version of this article.)

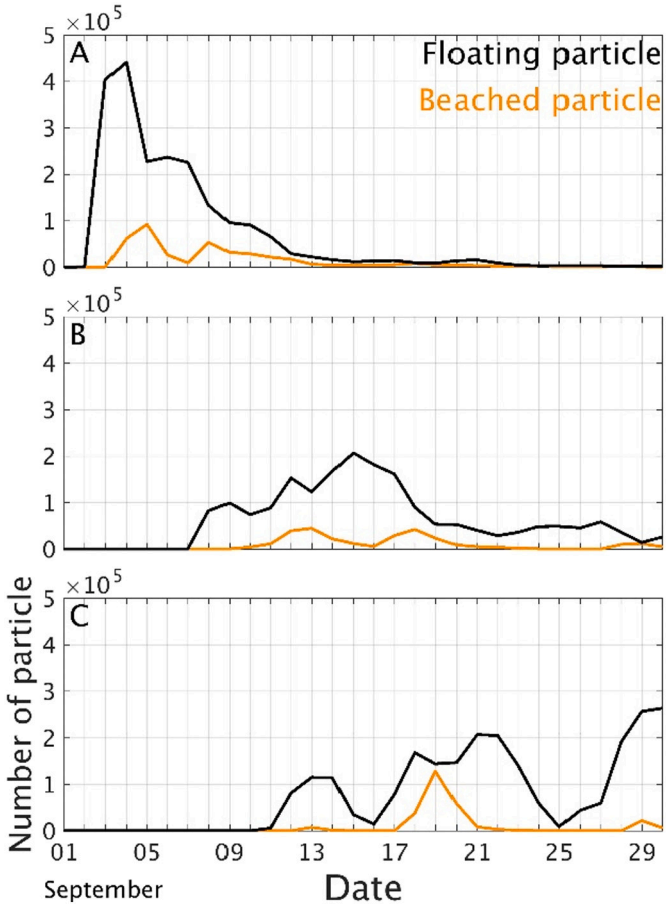

Fig. 10. Time series for the number of floating (black) and beached (orange) particles in the three colored boxes shown in Fig. 8. (For interpretation of the references to color in this figure legend, the reader is referred to the web version of this article.)

transported offshore and a narrower debris stream was formed. The leading edge of the CDOM plume was probably wider than that of TSS because of particle settlement, although this did not prevent the flood pulse from being tracked. The widths of the leading edges from the composite data were wider than that of the 0% windage scenario because of the offshore wind effects.

In summary, both the model outputs and satellite images showed southward movement along the coast, although there were some differences due to the windage acting on the debris of greater buoyancy and the lack of explicit freshwater plumes in the model.

3.4. Hotspots of debris accumulation

Using the composite images, the total numbers of particles that had beached in each coastal grid by October 20, 2016 (50 days after the initial release) were determined. As it took approximately 15 days for a particle to travel from the river mouth to 38°N, 50 days was deemed long enough to account for all the particles transported by the floodwaters. Particles arrived earlier on the northern coast but we focus on the cumulative effect here. The resolution of the input data was 0.08°, which was sufficient to capture the main geographical features of the coastline.

About 30% of the total particles released from the river beached within 50 km, and about 40% within 100 km of the river mouth, which is a similar finding to Atwood et al. (2019) who investigated particles from the Pho River, Italy, and Critchell et al. (2015), who examined fluvial debris on the east coast of Australia. Away from the river mouth, three areas were identified with large amounts of beached debris (marked by the green, blue, and black boxes in Fig. 9). These debris 'hotspots' are approximately 120 km, 280 km, and 420 km away from the river mouth, respectively. The highest numbers of beached particles in the grids in each hotspot, from north to south, were 105, 59, and 85 times that of the Gangneung grid, respectively.

Near the two northern hotspots (the green- and blue-boxed areas in Fig. 9, 'Hotspot A' and 'Hotspot B', respectively), currents flow toward

Table 2
Contribution (%) of beached particles from different windage scenarios in each hotspot shown in Fig. 8.

Hotspot	Windage								
	0.0%	0.5%	1.0%	1.5%	2.0%	2.5%	3.0%	3.5%	4.0%
A (green box)	10%	12%	13%	14%	14%	13%	11%	8%	6%
B (blue box)	34%	25%	17%	10%	6%	4%	2%	2%	1%
C (black box)	0%	2%	12%	24%	22%	14%	10%	9%	7%

the cape-shaped coast and the particles were easily accumulated here. To compare the effects of currents and wind, the proportion of beached particles associated with the different windage scenarios were calculated for the three hotspots (Table 2). As the wind effects become stronger, particles move further southward before reaching the coast. Thus, debris with lower windages accumulates more readily, especially in Hotspot B where the dominant wind blows alongshore. In the southernmost hotspot (the black-boxed area in Fig. 9, 'Hotspot C'), the currents do not flow toward the coast whereas the winds do blow onshore. Thus, the proportion of particles with a windage of <1% was very low while those with greater windages were more abundant. When the windage was increased to >2.5%, the proportion decreased slightly because fewer particles reached this area due to enhanced offshore dispersion in the upstream direction. In short, Hotspot C formed due to the prevailing onshore wind as noted by Critchell et al. (2015) and Moy et al. (2018), while the other two hotspots to the north formed due to the geometry of the coast and onshore currents. Time-series data for the numbers of beached particles and floating ones (Fig. 10) also showed the same tendency; in the two northern hotspots, the numbers of beached particles increased when the debris plume reached these locations whereas numbers increased in the southern hotspot both when the strength of the onshore wind was increased and the debris plume reached.

The method for hotspot devised by Atwood et al. (2019) cannot be applied to the CDOM and TSS anomalies. As the NKCC is a broadly permanent flow and the main efflux occurs during the rainy summer season, the mean distribution might be related to the flood-induced hotspots. The mean CDOM and TSS values (Fig. 5) were higher in the hotspot areas in the model. CDOM and TSS cannot be beached, but they could show areas where beaching is likely to occur. There was some discrepancy, however; the concertation was highest in East Korea Bay (Hotspot C) while Hotspot A, which is located further north, was the most prominent. Thus, from the mean CDOM and TSS hotspots could be identified but the beached amounts could not be quantified.

4. Conclusions

The debris released from the Tumen River due to Typhoon Lionrock in September 2016 was traced using GOCI satellite images and a Lagrangian particle-tracking model. The debris from the river was recorded approximately two weeks after the flood pulse at Gangneung, South Korea, 800 km south along the coast. As marine debris is typically too small to be observed directly using satellites, we traced the signature of the flood using CDOM and TSS. To differentiate between mean and flood-induced efflux, the images were decomposed into means and anomalies. Due to cloud there was not enough number of satellite images. The southward movements of the leading edges of the anomalies were then compared with the results from a particle-tracking model to validate the use of CDOM and TSS as debris-tracking variables and fill the gaps between the images. At the same time the images were used to validate the model results since the river is located in North Korea and it was impossible to obtain observation data. As a diverse range of debris types were released from the river, the windage effect varied in the model between 0% and 4% at 0.5% increments, and the 0% scenario and a composite of all the wind scenarios were compared to the satellite images.

The leading edges of the CDOM and TSS anomalies moved south along the east coast of the Korean Peninsula following the NKCC. As sediment settled to lower water layers downstream, the TSS anomalies became relatively weak compared to CDOM. This difference was not, however, significant enough to hinder the tracking of the floodwaters. The results of the particle-tracking model also showed that the debris from the river was transported south along the coast. The CDOM and TSS leading edges arrived at Gangneung approximately six days later than the debris in the composite analysis, which produced results similar to the observations. Thus, the rates of transport estimated from CDOM and TSS were approximately 30% lower. As CDOM and TSS are properties of water, they are not affected by the wind. On the other hand, debris floating at the surface can be strongly affected by wind. There is a wind component blowing parallel to the NKCC that would have accelerated the southward transport of the debris. The distributions of CDOM and TSS compared better with the 0% wind scenario than with the composite, although the transport of debris lagged behind CDOM and TSS in the 0% windage scenario by approximately one day. In the model, the freshwater plume from the river was not explicitly considered and the current due to mass flux from the river could be the cause of this discrepancy (Troselj et al., 2017; Urakawa et al., 2015). If one could conduct a high resolution plume modeling, and combine the results to those from a coarser resolution ocean model, it is possible to construct a velocity field with suitable coastal currents. This would be a next step for an operational debris prediction system. Overall, CDOM and TSS are more appropriate for tracking debris that is less affected by wind, such as completely submerged material.

The model identified hotspots of debris accumulation along the east coast of North Korea as the result of onshore currents and winds toward the cape-shaped coast. If wind is the main driver, debris with higher buoyancy would preferentially accumulate; if ocean currents are the main driver, debris with lower buoyancy will be favored. Although the hotspots cannot be verified due to a lack of observational data, considering the consistency between the model results and debris sighting at Gangneung, the model prediction is considered accurate. A comparison between the modeled hotspots and the mean values of CDOM and TSS (Fig. 5) suggests that these satellite-derived variables can be effectively used to locate hotspots of debris accumulation, as reported by Atwood et al. (2019), and even though they are located more than 100 km away from the river mouth.

Typhoons are expected to become more intense (Mei and Xie, 2016; Tsuboki et al., 2015) in the future due to global warming (Knutson et al., 2010). If so, flooding and the release of debris from land into the ocean will become more frequent, and the need to track and predict debris movement would consequently increase. Near to the mouths of rivers, debris patches can form, which could be tracked using spectral methods (Biermann et al., 2020; Topouzelis et al., 2019). Away from the mouths of rivers, debris patches become dispersed, rendering spectral-based tracking methods invalid. In such cases, indirect methods based on CDOM and TSS along with Lagrangian particle-tracking models can be effectively applied to trace debris movement as well as to estimate coastal debris accumulation. Our methodology is promising, but the lack of the observational validation for the hot spots located in North Korea remains as a limitation.

CRediT authorship contribution statement

Seongbong Seo: Data Curation, Data analysis, Visualization, Methodology, Formal analysis, Writing- Original draft preparation. **Young-Gyu Park**: Supervision, Conceptualization, Methodology, Formal analysis, Writing- Reviewing and Editing. **Kwangseok Kim**: Data Curation.

Declaration of competing interest

The authors declare that they have no known competing financial interests or personal relationships that could have appeared to influence the work reported in this paper.

Acknowledgements

This research was conducted as a part of Seongbong Seo's Ph.D. research. The work was funded through the projects "Environmental risk assessment of microplastic in the marine environment" and "Technology development for practical applications of multi-satellite data to maritime issues" from the Ministry of Oceans and Fisheries, Korea. We are grateful to the editor and anonymous reviewers for their constructive

comments.

References

Ahn, Y., Shanmugam, P., Moon, J., Ryu, J., 2008. Satellite remote sensing of a low-salinity water plume in the East China Sea. Ann. Geophys. 26 (7), 2019–2035.

Ahn, J.-H., Park, Y.-J., Ryu, J.-H., Lee, B., 2012. Development of atmospheric correction algorithm for Geostationary Ocean Color Imager (GOCI). Ocean Sci. J. 47 (3), 247–259.

Atwood, E.C., Falcieri, F.M., Piehl, S., Bochow, M., Matthies, M., Franke, J., Carniel, S., Sclavo, M., Laforsch, C., Siegert, F., 2019. Coastal accumulation of microplastic particles emitted from the Po River, Northern Italy: comparing remote sensing and hydrodynamic modelling with in situ sample collections. Mar. Pollut. Bull. 138, 561–574.

Baeye, M., Quinn, R., Deleu, S., Fettweis, M., 2016. Detection of shipwrecks in ocean colour satellite imagery. J. Archaeol. Sci. 66, 1–6.

Bai, Y., Pan, D., Cai, W.J., He, X., Wang, D., Tao, B., Zhu, Q., 2013. Remote sensing of salinity from satellite-derived CDOM in the Changjiang River dominated East China Sea. J. Geophys. Res. 118, 227–243.

Biermann, L., Clewley, D., Martinez-Vicente, V., Topouzelis, K., 2020. Finding plastic patches in coastal waters using optical satellite data. Sci. Rep. 10 (1), 1–10.

Burenkov, V., Goldin, Y.A., Kravchishina, M., 2010. The distribution of the suspended matter concentration in the Kara Sea in September 2007 based on ship and satellite data. Oceanology 50 (5), 798–805.

Choi, J.-K., Park, Y.J., Lee, B.R., Eom, J., Moon, J.-E., Ryu, J.-H., 2014. Application of the Geostationary Ocean Color Imager (GOCI) to mapping the temporal dynamics of coastal water turbidity. Remote Sens. Environ. 146, 24–35.

Choi, J.-G., Jo, Y.-H., Moon, I.-J., Park, J., Kim, D.-W., Lippmann, T.C., 2018. Physical forces determine the annual bloom intensity of the giant jellyfish Nemopilema nomurai off the coast of Korea. Reg. Stud. Mar. Sci. 24, 55–65.

Critchell, K., Grech, A., Schlaefer, J., Andutta, F., Lambrechts, J., Wolanski, E., Hamann, M., 2015. Modelling the fate of marine debris along a complex shoreline: lessons from the Great Barrier Reef. Estuar. Coast. Shelf Sci. 167, 414–426.

Del Castillo, C.E., Miller, R.L., 2008. On the use of ocean color remote sensing to measure the transport of dissolved organic carbon by the Mississippi River Plume. Remote Sens. Environ. 112 (3), 836–844.

Dormand, J.R., Prince, P.J., 1980. A family of embedded Runge-Kutta formulae. J. Comput. Appl. Math. 6 (1), 19–26.

Duhec, A.V., Jeanne, R.F., Maximenko, N., Hafner, J., 2015. Composition and potential origin of marine debris stranded in the Western Indian Ocean on remote Alphonse Island, Seychelles. Mar. Pollut. Bull. 96 (1–2), 76–86.

Eriksen, M., Lebreton, L.C., Carson, H.S., Thiel, M., Moore, C.J., Borerro, J.C., Galgani, F., Ryan, P.G., Reisser, J., 2014. Plastic pollution in the world's oceans: more than 5 trillion plastic pieces weighing over 250,000 tons afloat at sea. PLoS ONE 9 (12), e111913.

Fournier, S., Lee, T., Gierach, M.M., 2016. Seasonal and interannual variations of sea surface salinity associated with the Mississippi River plume observed by SMOS and Aquarius. Remote Sens. Environ. 180, 431–439.

Hall, K., 2000. Impacts of Marine Debris and Oil: Economic and Social Costs to Coastal Communities. Kommunenes Internasjonale Miljøorganisasjon (KIMO) (ISBN 0904562891).

Isobe, A., 2005. Ballooning of river-plume bulge and its stabilization by tidal currents. J. Phys. Oceanogr. 35 (12), 2337–2351.

Isobe, A., Isoda, Y., 1997. Circulation in the Japan Basin, the northern part of the Japan Sea. J. Oceanogr. 53, 373–382.

Isobe, A., Kako, S.I., Chang, P.-H., Matsuno, T., 2009. Two-way particle-tracking model for specifying sources of drifting objects: application to the East China Sea Shelf. J. Atmos. Ocean. Technol. 26 (8), 1672–1682.

Iwasaki, S., Isobe, A., Kako, S.I., Uchida, K., Tokai, T., 2017. Fate of microplastics and mesoplastics carried by surface currents and wind waves: a numerical model approach in the Sea of Japan. Mar. Pollut. Bull. 121 (1–2), 85–96.

Jang, Y.C., Hong, S., Lee, J., Lee, M.J., Shim, W.J., 2014. Estimation of lost tourism revenue in Geoje Island from the 2011 marine debris pollution event in South Korea. Mar. Pollut. Bull. 81 (1), 49–54.

Kim, Y.-J., Yoon, J.S., 2009. A study on the behavior of floating debris and fresh water diffusion according to discharge of Namgang Dam. J. Ocean Eng. Technol 23 (2), 37–46.

Knutson, T.R., McBride, J.L., Chan, J., Emanuel, K., Holland, G., Landsea, C., Held, I., Kossin, J.P., Srivastava, A.K., Sugi, M., 2010. Tropical cyclones and climate change. Nat. Geosci. 3 (3), 157–163.

Kwan, C., Qi, H., Tran, T., 2016. Recent advances in remote spectral sensing. J, Sensors 2016.

Lebreton, L.-M., Greer, S., Borrero, J.C., 2012. Numerical modelling of floating debris in the world's oceans. Mar. Pollut. Bull. 64 (3), 653–661.

Lebreton, L., Slat, B., Ferrari, F., Sainte-Rose, B., Aitken, J., Marthouse, R., Hajbane, S., Cunsolo, S., Schwarz, A., Levivier, A., Noble, K., Debeljak, P., Maral, H., Schoeneich-Argent, R., Brambini, R., Reisser, J., 2018. Evidence that the Great Pacific Garbage Patch is rapidly accumulating plastic. Sci. Rep. 8 (1), 4666.

Lee, J., 2016a. Where did the wood debris covering Gangneung Sodol Beach come from. https://www.yna.co.kr/view/AKR20160917034600062. (Accessed 6 November 2020). in Korean.

Lee, S., 2016b. Emergency budget support for the collection of 300 tons of debris from North Korea and China that came to the east coast of Korea. https://www.dailian.co.kr/news/view/590783. (Accessed 6 November 2020). in Korean.

Mansui, J., Molcard, A., Ourmieres, Y., 2015. Modelling the transport and accumulation of floating marine debris in the Mediterranean basin. Mar. Pollut. Bull. 91 (1), 249–257.

Marta-Almeida, M., Mendes, R., Amorim, F.N., Cirano, M., Dias, J.M., 2016. Fundão Dam collapse: oceanic dispersion of River Doce after the greatest Brazilian environmental accident. Mar. Pollut. Bull. 112 (1–2), 359–364.

Maximenko, N., MacFadyen, A., Kamachi, M., 2015. Modeling the drift of marine debris generated by the 2011 tsunami in Japan. PICES Press 23 (2), 32–36.

McIlgorm, A., Campbell, H.F., Rule, M.J., 2011. The economic cost and control of marine debris damage in the Asia-Pacific region. Ocean Coast. Manag. 54 (9), 643–651.

Mei, W., Xie, S.P., 2016. Intensification of landfalling typhoons over the northwest Pacific since the late 1970s. Nat. Geosci. 9 (10), 753–757.

Moy, K., Neilson, B., Chung, A., Meadows, A., Castrence, M., Ambagis, S., Davidson, K., 2018. Mapping coastal marine debris using aerial imagery and spatial analysis. Mar. Pollut. Bull. 132, 52–59.

Nelson, N., Siegel, D., Michaels, A., 1998. Seasonal dynamics of colored dissolved material in the Sargasso Sea. Deep Sea Res. Part I Oceanogr. Res. Pap. 45 (6), 931–957.

Neumann, D., Callies, U., Matthies, M., 2014. Marine litter ensemble transport simulations in the southern North Sea. Mar. Pollut. Bull. 86 (1–2), 219–228.

North, E., Hood, R., Chao, S.-Y., Sanford, L., 2006. Using a random displacement model to simulate turbulent particle motion in a baroclinic frontal zone: a new implementation scheme and model performance tests. J. Mar. Syst. 60 (3–4), 365–380.

Osadchiev, A., 2015. A method for quantifying freshwater discharge rates from satellite observations and Lagrangian numerical modeling of river plumes. Environ. Res. Lett. 10 (8), 085009.

Osburn, C.L., Retamal, L., Vincent, W.F., 2009. Photoreactivity of chromophoric dissolved organic matter transported by the Mackenzie River to the Beaufort Sea. Mar. Chem. 115 (1–2), 10–20.

Rudorff, N., Rudorff, C.M., Kampel, M., Ortiz, G., 2018. Remote sensing monitoring of the impact of a major mining wastewater disaster on the turbidity of the Doce River plume off the eastern Brazilian coast. ISPRS J. Photogramm. Remote Sens. 145, 349–361.

Ryu, J.-H., Han, H.-J., Cho, S., Park, Y.-J., Ahn, Y.-H., 2012. Overview of geostationary ocean color imager (GOCI) and GOCI data processing system (GDPS). Ocean Sci. J. 47 (3), 223–233.

Seo, S., Park, Y.-G., 2020. Destination of floating plastic debris released from ten major rivers around the Korean Peninsula. Environ. Int. 138, 105655.

Seung, Y.-H., Kim, K., 1989. On the possible role of local thermal forcing on the Japan Sea circulation. J. Oceanol. Soc. Korea 24, 29–38.

Smagorinsky, J., 1963. General circulation experiments with the primitive equations: I. The basic experiment. Mon. Weather Rev. 91 (3), 99–164.

Tishchenko, P.Y., Semkin, P.Y., Pavlova, G.Y., Tishchenko, P., Lobanov, V., Marjash, A., Mikhailik, T.A., Sagalaev, S.G., Sergeev, A.F., Tibenko, E.Yu., Khodorenko, N.D., Chichkin, R.V., Shvetsova, M.G., Shkirnikova, E.M., 2018. Hydrochemistry of the Tumen River Estuary, Sea of Japan. Oceanology 58 (2), 175–186.

Topouzelis, K., Papakonstantinou, A., Garaba, S.P., 2019. Detection of floating plastics from satellite and unmanned aerial systems (Plastic Litter Project 2018). Int. J. Appl. Earth Obs. Geoinf. 79, 175–183.

Troselj, J., Sayama, T., Varlamov, S.M., Sasaki, T., Racault, M.F., Takara, K., Miyazawa, Y., Kuroki, R., Yamagata, T., Yamashiki, Y., 2017. Modeling of extreme freshwater outflow from the north-eastern Japanese river basins to western Pacific Ocean. J. Hydrol. 555, 956–970.

Tsuboki, K., Yoshioka, M.K., Shinoda, T., Kato, M., Kanada, S., Kitoh, A., 2015. Future increase of supertyphoon intensity associated with climate change. Geophys. Res. Lett. 42 (2), 646–652.

Urakawa, L.S., Kurogi, M., Yoshimura, K., Hasumi, H., 2015. Modeling low salinity waters along the coast around Japan using a high-resolution river discharge dataset. J. Oceanogr. 71 (6), 715–739.

van Sebille, E., Wilcox, C., Lebreton, L., Maximenko, N., Hardesty, B.D., Van Franeker, J. A., Eriksen, M., Siegel, D., Galgani, F., Law, K.L., 2015. A global inventory of small floating plastic debris. Environ. Res. Lett. 10 (12), 124006.

Vodacek, A., Blough, N.V., DeGrandpre, M.D., Nelson, R.K., 1997. Seasonal variation of CDOM and DOC in the Middle Atlantic Bight: terrestrial inputs and photooxidation. Limnol. Oceanogr. 42 (4), 674–686.

Wang, X., Zou, Y., He, X., 2018. Evaluation of ocean forecasting in the East China Sea. In: Liang, X.S., Zhang, Y. (Eds.), Coastal Environment, Disaster, and Infrastructure-A Case Study of China's Coastline. IntechOpen, London, pp. 259–272.

Warrick, J.A., DiGiacomo, P.M., Weisberg, S.B., Nezlin, N.P., Mengel, M., Jones, B.H., Ohlmann, J.C., Washburn, L., Terrill, E.J., Farnsworth, K.L., 2007. River plume patterns and dynamics within the Southern California Bight. Cont. Shelf Res. 27 (19), 2427–2448.

Wu, H., Adler, R.F., Tian, Y., Huffman, G.J., Li, H., Wang, J., 2014. Real-time global flood estimation using satellite-based precipitation and a coupled land surface and routing model. Water Resour. Res. 50 (3), 2693–2717.

Yoo, C.-I., Yoon, H.-S., Kim, G.-T., 2007. The behavior of floating debris in the Nakdong River Estuary using a simple numerical particle model. J. Korean Soc. Mar. Environ. Saf. 13 (4), 9–14.

Yoon, J.-H., Kim, Y.-J., 2009. Review on the seasonal variation of the surface circulation in the Japan/East Sea. J. Mar. Syst. 78 (2), 226–236.

Yoon, J.-H., Kawano, S., Igawa, S., 2010. Modeling of marine litter drift and beaching in the Japan Sea. Mar. Pollut. Bull. 60 (3), 448–463.